

Effect of thermosolutal convection on directional solidification

SURESH V GARIMELLA* and JAMES E SIMPSON

School of Mechanical Engineering, Purdue University, West Lafayette,
IN 47907-1288, USA
e-mail: sureshg@ecn.purdue.edu

Abstract. The impact of thermosolutal convection during directional solidification is explored via results of numerical investigations. Results from fully transient numerical simulations of directional solidification in a differentially heated cavity under terrestrial conditions and Bridgman crystal growth in space are discussed. The pivotal role of *both* thermal *and* solutal convection in the solidification process is illustrated by examining these two cases. In particular, radial and longitudinal macrosegregation resulting from this thermosolutal convection is discussed.

Keywords. Thermosolutal convection; directional solidification; macrosegregation.

1. Introduction

Increasing demand for high-quality materials for use in the aerospace, optical, biomedical and electronic fields has led to an increased level of interest in the processes used to synthesize these advanced materials. When an alloy melt is solidified by heat removal primarily in one direction, a homogeneous casting is produced with columnar grains aligned in the primary growth direction and few transverse grain boundaries. The material produced by this process of *directional solidification* has enhanced properties such as improved thermal fatigue strength, increased rupture strain and more uniform electrical and thermal properties. However, these castings may be characterized by large-scale inhomogeneities in the form of radial and longitudinal macrosegregation (Smith *et al* 1955; Flemings & Nereo 1967). The geometry of the melt region, and transport parameters such as the rate of solidification, solute rejection at the advancing solid/liquid interface and convective flow in the melt determine the solute distribution, and hence the macrosegregation, in the solidified material. Knowledge of the momentum, heat and species transport processes during solidification is essential for reducing macrosegregation (Adornato & Brown 1987).

Natural convection arises as a result of gravity acting upon density differences in the melt. While the effect of natural convection due to thermal buoyancy forces has been

*For correspondence

A list of papers is given at the end of the paper

studied extensively for pure materials, there has been less work on the more complex case of alloy solidification where buoyancy forces occur due to *both* thermal and solutal gradients. In the latter case, this *thermosolutal* convection often results in complex convection patterns which evolve with time. It is these complex convective motions which influence the homogeneity of the alloy casting, and therefore, they need to be resolved effectively.

Numerical simulation of solidification processes is a potentially valuable tool for the design and control of crystal growth systems. Not only is computer modelling a more convenient and cost-effective technique than experimentation, but quantities which directly affect the process and are difficult or impossible to measure in experiments can be determined from simulations. Velocities and solute distributions in the opaque, high-temperature and highly reactive metallic melts are examples of such critical quantities. Many numerical models have been developed for the simulation of solidification in transparent salt systems (a review of the more popular models is given by Oldenberg & Spera 1991). The numerical simulation of metals is much more challenging since metallic melts are characterized by low Prandtl numbers and high levels of convection (Hyun *et al* 1995). Only recently have suitable techniques become available for the simulation of solidification involving metallic systems that include all the key details of the process while keeping computational costs low (Zhang *et al* 1996; Simpson & Garimella 1998).

The aim of this paper is to detail the influence of thermosolutal convection on the solidification process. The results from numerical simulations for two directional solidification processes are presented and discussed. The first series of simulations examine the directional solidification of pure Sn and a Sn–Bi alloy system under terrestrial (earth gravity) conditions (Simpson & Garimella 1998). It will be seen that large levels of thermal convection distort the interface and result in significant macrosegregation levels. The second series of simulations examine the fully transient crystal growth of a Bi–Sn alloy under microgravity (space) conditions by the Bridgman process (Simpson *et al* 2001). It will be seen that despite the significantly reduced level of gravity, thermosolutal convection results in measurable levels of radial segregation.

2. Analysis

The problem under consideration is directional solidification of a binary alloy either in a closed mould under terrestrial conditions or by the Bridgman process in space, as shown schematically in figures 1a and b respectively. The melt region is considered to be a viscous Newtonian fluid subject to thermosolutal convection. Thermophysical properties are considered to be constant but distinct for the solid and liquid phases. Density variations are assumed to be subject to the Boussinesq approximation. The governing equations for the velocity field are the vorticity and vector potential equations which are (Roache 1976):

$$(\partial \bar{\zeta} / \partial t) + \nabla \times (\bar{\zeta} \times \bar{u}) = -\nabla \times (T - T_c) \bar{g} - \nabla \times (C - C_0) \bar{g} + \nu \nabla^2 \bar{\zeta}, \quad (1)$$

$$\nabla^2 \bar{\psi} = -\bar{\zeta}. \quad (2)$$

In these equations, the definition of vorticity and the relationship between velocity and vector potential are

$$\bar{\zeta} = -\nabla \times \bar{u}, \quad \bar{u} = \nabla \times \bar{\psi}. \quad (3)$$

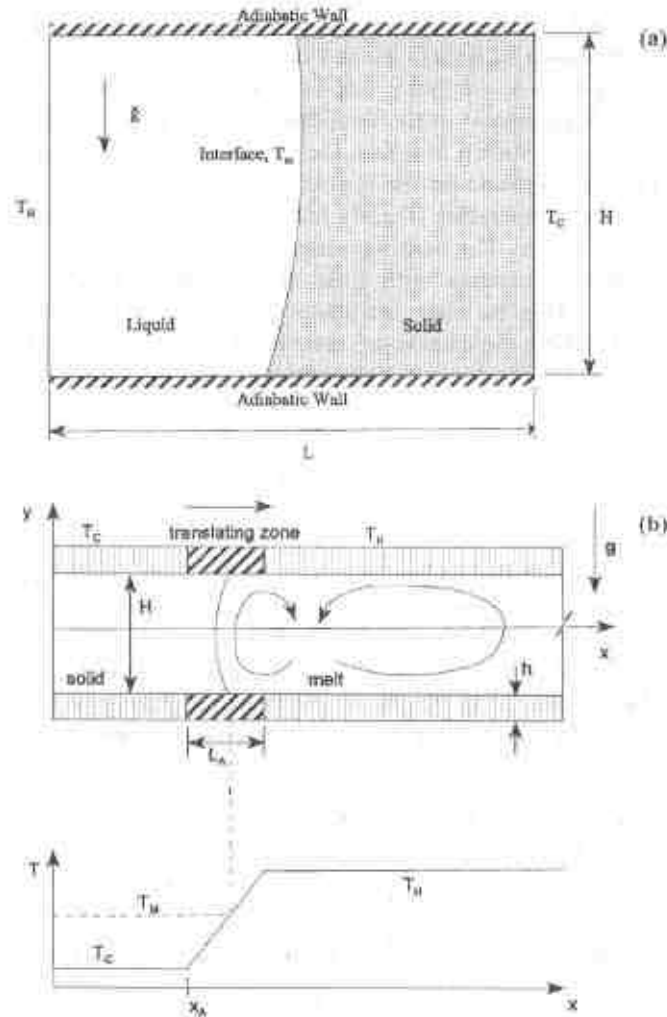


Figure 1. Computational domain and boundary conditions for (a) directional solidification in a differentially heated cavity under terrestrial conditions, and (b) space-borne Bridgman crystal growth process.

For a non-slip wall, the boundary conditions to be imposed on vorticity (Hirasaki & Hellums 1968) are that the velocity be zero, as also the tangential derivatives of its components, while the vector potential at a plane, impermeable surface be normal to the surface and its gradient, zero. As an initial condition, the fluid must be quiescent (zero potential and vorticity everywhere).

The governing equation for the conservation of energy for phase-change problems may be expressed as

$$A(T, C)(\partial T / \partial t) + \rho c_{pL} \nabla \cdot (\mathbf{u}\theta) = \nabla \cdot (k \nabla T) + B(T, C). \quad (4)$$

It will be seen below that effective heat capacity A and source term B are specified in order to include phase-change. An initial temperature equal to the hot wall temperature is applied

throughout the flow field. The thermal boundary conditions for the solidification systems being investigated are shown in figures 1a and b.

The conditions along the $y = -h$ and $y = H + h$ walls required for the Bridgman process are functions of time. A schematic of the temperature imposed at these boundaries, which approximates the furnace, is shown in figure 1b. There is a translating zone (considered an 'adiabatic' zone if the temperature profile is unknown) between the hot and cold regions of the furnace, in which the temperature linearly increases from the cold furnace temperature to the hot furnace temperature. The melting temperature of the material occurs somewhere within this zone, which translates with time at a constant x -velocity, known as the *translation velocity*, u_t . This is what facilitates the directional growth of the crystal. Defining the x location where the translating zone meets the cold furnace temperature zone to be at $x_A(t)$, the boundary condition for temperature may be expressed as

$$\text{at } y = -h, H + h: \quad T = \begin{cases} T_C, & \text{for } x < x_A(t), \\ T_C + \Delta T(x - x_A(t))/L_A, & \text{for } x_A(t) \leq x \leq [x_A(t) + L_A], \\ T_H, & \text{for } x_A(t) < x. \end{cases} \quad (5)$$

In principle, the solution of the energy equation (4) coupled with the solution of the vorticity–vector potential equations (1) and (2) would yield the temperature and velocity distribution throughout the simulation domain. However, the problem of modelling the physics of the propagation of the solidification front and determining its location remains to be addressed. We choose to do this by employing the phase-transformation model of Zeng & Faghri (1994). For the present study, concentration dependence on temperature is neglected; terms A and B may be written as

$$\begin{aligned} A(T) &= \rho(c_{pl}f_L + c_{ps}f_S + a(T)(\partial f_L/\partial T)), \\ B(T) &= -a(T)(\partial f_L/\partial t), \\ a(T) &= \rho[(c_{pl} - c_{ps})T + \Delta H]. \end{aligned} \quad (6)$$

The equation for conservation of solute throughout the computational domain is

$$(\partial C_L/\partial t) + \nabla \cdot (\bar{u}C_L) = D\nabla^2 C_L + S(T, C_L). \quad (7)$$

This equation is analogous to the energy equation. We impose an initial solute concentration throughout the solution domain. For both systems the boundary conditions are identical: the mould boundaries are impermeable to solute.

Again, in principle, solution of (7) along with energy equation (4) and vorticity–vector potential equations (1) and (2) all subject to the relevant boundary and initial conditions are enough to determine the solute, temperature and velocity values throughout the solution domain. However, the more general problem involving phase change demands that the thermodynamics of solute redistribution be addressed. Following the work of Swaminathan & Voller (1997) and Voller *et al.* (1989), source term S may be written as the differential,

$$S(T, C) = \frac{\partial (f_L C_L)}{\partial t} + k_p C_L \frac{\partial f_S}{\partial t}. \quad (8)$$

The computational domain is primarily discretized using regularly spaced finite-difference mesh points. Superimposed on this grid are finite volumes which are used for the solution for the energy and species concentration equations. The finite-volume centres are

staggered with respect to the finite-difference mesh point locations. Vorticity, velocity and vector potential are calculated at the finite-difference mesh points. Temperature and solute concentration are evaluated at the control volume centres. Further details of the numerical solution schemes for solving the terrestrial directional solidification problem (figure 1a) and the space crystal growth case (figure 1b) may be found in Simpson & Garimella (1998) and Simpson *et al* (2001) respectively, and are not provided here.

3. Results and discussion

3.1 Directional solidification of pure tin

In order to compare the existing solution scheme with numerical and experimental data from the literature (Wolff & Viskanta 1988; Raw & Lee 1991; Zhang *et al* 1996), simulations for the solidification of pure tin in a differentially heated cavity with an aspect ratio (H/L) of 0.75 were performed. The important physical parameters for this case are $L = 8.89$ cm, $Ra (= Gr \times Pr) = 1.4 \times 10^5$, $Pr = 0.017$, $T_H = 233^\circ\text{C}$, $T_C = 229^\circ\text{C}$, $\Delta H = 59 \times 10^3$ J/kg K, and $c_p = 255$ J/kgK. Thermophysical properties for the liquid phase are considered to be constant and equal to those in the solid phase. A 61×46 mesh was used.

Isotherms and velocity vectors at $t = 1.896$ h for the solidification process are shown in figure 2. At this time the solidification front has propagated well into the melt, with over half the cavity consisting of solid tin. The velocity vectors show that two convective cells have formed at this time. The primary recirculating zone is at the top of the melt. A single convection cell cannot be sustained in the presence of the sloping interface and weakening natural convection (due to the locally decreased melt size). Thus the lower cell forms,

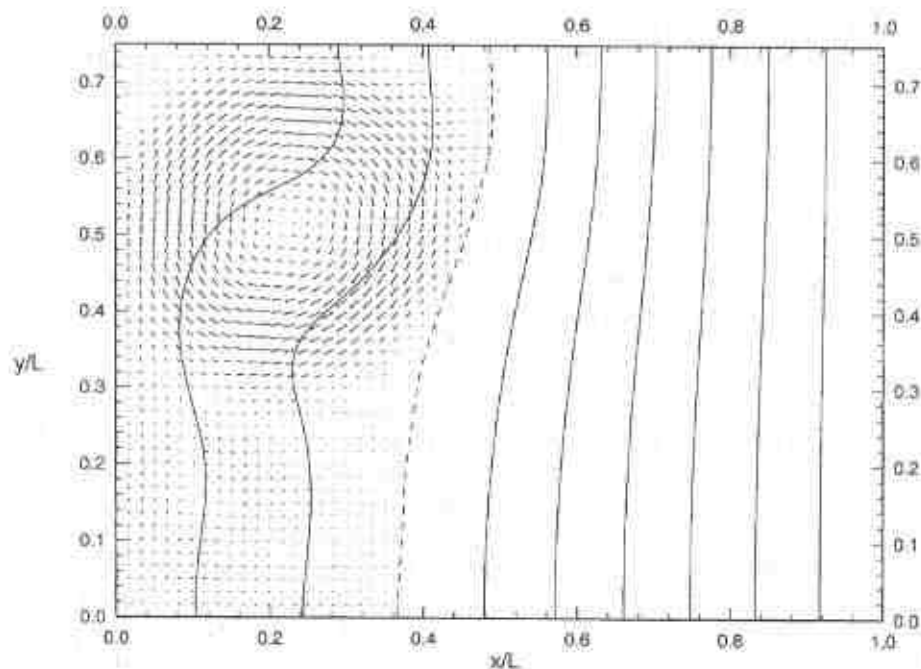


Figure 2. Velocity vectors and isotherms for pure Sn at $t = 1.896$ h.

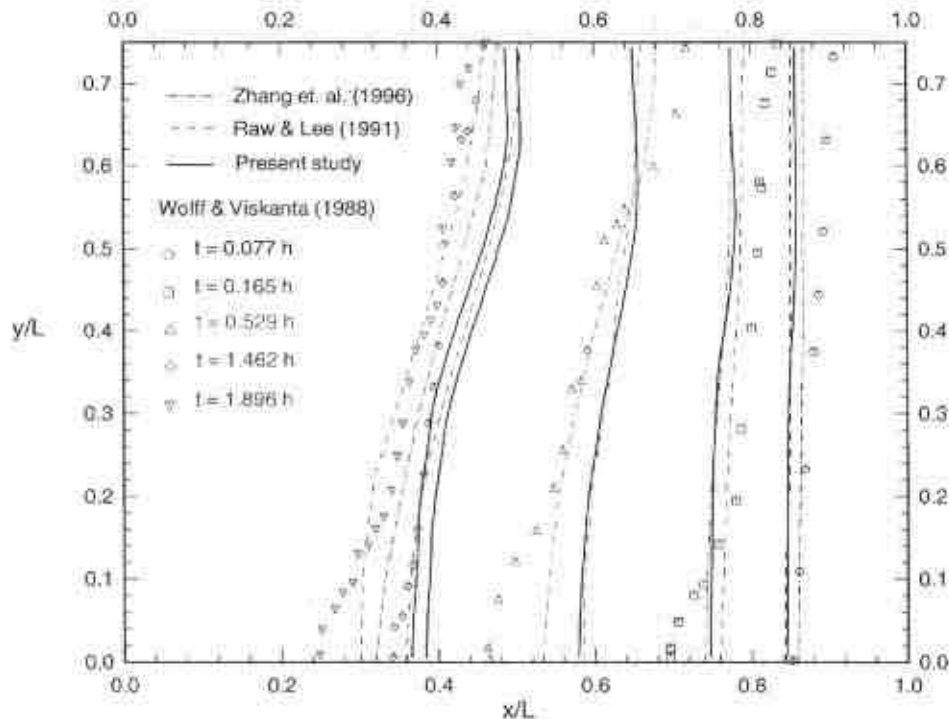


Figure 3. Comparison of experimentally determined and numerically predicted front locations.

circulating in the same direction as the primary cell and entraining cold recirculating fluid from the primary cell. A similar convective pattern is indicated in the results of Dantzig (1989) for a simulation of the melting of pure gallium when the melt region is of a similar shape.

The predicted solidification front locations from the present study are compared to experimental data (Wolff & Viskanta 1988) and numerical predictions in the literature (Raw & Lee 1991; Zhang *et al.* 1996) in figure 3. The current predictions are in acceptable agreement with the experimental results. At times $t = 0.077$ and 0.165 h, the solidification front has propagated quite rapidly, controlled primarily by the action of conduction at the chilled wall. Some convective effects are in play since the front is not vertical. The predicted front location from the numerical analysis at these early times is further advanced compared to the experimental results. At time $t = 0.077$ h the mid-point of the front is 15% further advanced compared to the experimental value; and at time $t = 0.165$ h this value is 6%. This discrepancy in front location may be explained by the observations of Wolff & Viskanta (1988) on the thermal inertia of the experimental apparatus. The apparatus was not capable of producing an instantaneous temperature drop to T_c at the cold wall at time $t = 0$; in fact 0.033 h elapsed before the cold plate temperature reached T_c . At later times, the predicted front location tends to lag behind the experimentally determined location. Also, the numerical results fail to predict the increased thickness of the front at the bottom of the cavity. Both these discrepancies may be attributed to the imperfect insulating material at the bottom of the experimental apparatus (Wolff & Viskanta 1988). The other numerical results exhibit similar discrepancies when compared to the experiments.

The CPU requirement for this simulation was approximately 3.5 h on a DEC 3000/700 (225 MHz, Specfp95 5.71) for a mesh of 61×46 . This compares with the two-domain approach of Zhang *et al.* (1996) which required 45 h on a Sun Sparc 10 workstation for a transforming mesh of 42×42 points, and with that of Raw & Lee (1991) which required 0.73 h on a CDC Cyber 840 supercomputer for a single-domain solution with a fixed mesh of 41×31 points.

3.2 Simulation of terrestrial Sn-Bi alloy solidification

Simulations for the solidification of a Sn-Bi binary alloy system were performed. In order to effect a tractable buoyancy ratio that causes laminar rather than turbulent convection, the dimensions of the solution domain and the temperature difference were altered from the case of pure tin above to: $L=5$ cm, $T_c=217.9^\circ\text{C}$, $T_H=237.9^\circ\text{C}$. The initial solute concentration was 0.5% Bi; in addition, $Le=4.0 \times 10^3$, $k_p=0.36$; R_H (buoyancy ratio) ($=Gr_s/Gr$) = 5.05. Thermophysical properties used were as those for pure tin, and cavity aspect ratio was maintained at 0.75. An additional simulation was performed for pure tin using the new temperature difference and cavity dimensions to provide a basis for comparison of the alloy results. The CPU time required for 10,000 time steps (real time $t=0.621$ hours) was 1.2 hours.

At $t=0.062$ h, the results (not shown here) were similar in character to those for pure tin. However, the strength of convection was smaller than that at the corresponding time for pure tin. Since bismuth has a higher density than tin, once the solute has been distributed throughout the flow field by thermal convection, it acts to oppose that convection and hence retard the action of the thermal convective cell.

Figure 4a shows the isotherms and velocity vectors at a later time, $t=0.6207$ h. The results are again similar in character to those found for pure tin. The convection in the primary recirculation is weaker than for pure tin. Interestingly, the secondary recirculation exhibits higher convection levels.

Figure 4b is a plot of lines of constant solute concentration in the melt. The average concentration in the bulk of the melt has risen to approximately 0.72% from the initial value of 0.5% as the front has propagated into the melt, rejecting solute-rich fluid at the interface which is then convected throughout the melt. The lines of constant solute concentration clearly indicate the influence of the convection patterns on the distribution of the solute.

3.3 Space crystal growth of a Bi-0.1 at.% Sn alloy

For simulating the Bridgman crystal growth of a Bi-0.1 at.% Sn (0.08185 vol.% Sn) alloy, the thermophysical properties used were those of pure bismuth from Yao *et al.* (1995). The cold and hot furnace temperatures were $T_c=50^\circ\text{C}$ and $T_H=700^\circ\text{C}$ respectively. Liquid properties were used as the reference properties for the nondimensionalization scheme. The properties for solid and liquid bismuth were evaluated at the mean solid and the mean liquid temperatures of 160.7°C and 485.7°C respectively. The reference density was considered to be equal for both phases. The property values were: $k_s=6.872$ W/mK, $k_l=14.66$ W/mK, $\rho_0=10,070$ kg/m³, $c_{ps}=132.6$ J/kgK, $c_{pl}=135.3$ J/kgK, $\Delta H=52.3$ kJ/kg, $\mu=1.240 \times 10^{-3}$ Ns/m, and $T_m=271.3^\circ\text{C}$. The thermal expansivity of the liquid was taken to be $\beta_l=-1.25 \times 10^{-4}$ K⁻¹. The properties used for the fused silica ampoule wall were $k_w=2.10$ W/mK, $\rho_w=2,020$ kg/m³, $c_{pw}=1066.8$ J/kgK. The dimensions used to

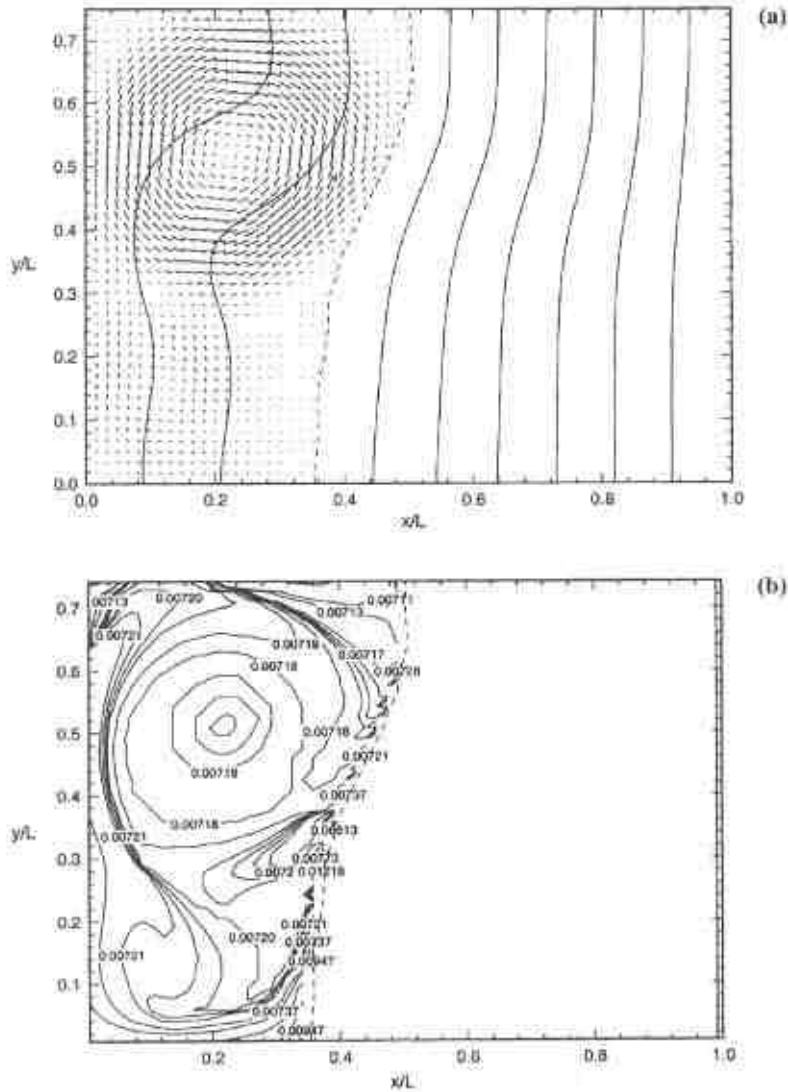


Figure 4. (a) Velocity vectors and isotherms, and (b) isolines, for bismuth concentration in the melt for Sn-0.5% Bi at $t=0.621$ h. In (a) the isotherms are at intervals of $\Delta\theta=0.1$. Dashed line is front location.

define the domain were $H=6$ mm and $L=75$ mm. The ampoule wall thickness, h , was 2 mm. The length of the insulated translating zone was $L_A=25$ mm, with a translation velocity of $u_t=3.38$ $\mu\text{m/s}$. The gravity level was 10 μg , with gravity acting in the negative y direction. In addition, the value for diffusivity of liquid Sn in liquid Bi was $D=3.50 \times 10^{-9}$ m^2/s , and the partition coefficient was $k_p=0.029$. The value of solutal expansion coefficient was taken to be $\beta_c=-0.305$ $(\text{vol.}\%)^{-1}$. The diffusivity value was calculated at the mean melt temperature. The liquid composition was taken to be at a uniform value of 0.1 vol.% as the initial condition. These values result in important nondimensional quantities $\text{Gr}=113.6$, $\text{Pr}=0.01144$, $R_B=3.072 \times 10^{-2}$ ($\text{Gr}_s=0.3490$)

and $Le = 3074$. The numerical model used for the results presented here has also been used to investigate the influence of gravity levels on space crystal growth (Simpson & Garimella 1999), the impact of the presence of a capillary tube on the process (Simpson *et al* 1999a) and as the computational component of a combined experimental and numerical investigation into the Bridgman growth of transparent metal analogs (Simpson *et al* 1999b,c).

Velocity vectors and isotherms after 3,000 s are shown for this alloy in figure 5a. Note that velocity vectors are shown at every other mesh point for this and subsequent vector plots. A single, counter-clockwise, thermally driven convective cell dominates the velocity plot. The maximum u -velocity is $3.467 \mu\text{m/s}$ at $(24.75, -1.8 \text{ mm})$. The magnitude of the maximum v -velocity is $-1.768 \mu\text{m/s}$ at $(17.75, 0 \text{ mm})$ acting in the negative y direction. The thermal field is not distorted by the action of convection. Figure 5b shows results at 6,000 s. The magnitude of the maximum v -velocity has decreased to $-1.720 \mu\text{m/s}$ acting downward at $(28.125, 0 \text{ mm})$. This is a result of solute rejection at the interface: the lighter solute accumulates near the interface and opposes the increase in density caused by lower temperatures in this region, thus retarding the velocities in the thermally induced convective cell. At a later time (9,000 s, figure 5c), the maximum v -velocity is $-1.649 \mu\text{m/s}$ (at $38.275, 0 \text{ mm}$) confirming the trend of solute rejection opposing the convective motion due to the applied temperature gradient.

Traces of solute concentration across the height of solidified alloy in the domain are shown in figure 6a. Three different x -locations (16.18, 26.30, 36.41 mm) are shown; these locations correspond to the location of the interface at $y = 0$ at times of 3,000, 6,000 and 9,000 s respectively. To aid in visualizing the influence of convection, results for a simulation involving diffusion only (no convection) are superimposed on this plot. Note that these pure diffusion results indicate that significant radial segregation arises due to interface curvature (see Adornato & Brown 1987, Liang & Lan 1996) such that the values for solute concentration at the centreline are larger than those at the edges. The level of curvature-induced radial segregation remains almost constant, with values of $\xi = 29.1\%$ (based on the mean concentration) at $x = 16.18 \text{ mm}$ and 29.4% at $x = 26.30$ and 36.41 mm . The inclusion of convection into the calculations causes the following effects. Solute levels are increased for low values of y and decreased for higher values of y . Furthermore, the y -location at which the maximum value for solute concentration is found is shifted from the centreline to $y = -1.234 \text{ mm}$ for all the traces shown. This is a consequence of the convective flow sweeping solute "down" the interface in the direction of decreasing y and away from the interface in the direction of increasing x (refer to figure 5). The maximum values for solute concentration are $C_{\text{max}}/C_0 = 0.2953, 0.4971, 0.6496$ for the traces at $x = 16.18, 26.30$ and 36.41 mm respectively. The radial segregation values increase slightly from $\xi = 50.1\%$ at $x = 16.18 \text{ mm}$ to 56.3% at $x = 36.41 \text{ mm}$.

Traces of solute concentrations in the solid and melt at times of 3,000, 6,000 and 9,000 s are shown in figure 6b. These traces run longitudinally along the ampoule for three different heights of $y = -2.88, 0$ and 2.88 mm . Note that the interface location on the centreline ($y = 0$) traces lags slightly behind the value for the other traces since the interface is curved. Solute build-up near the interface, and the exponential profile characteristic of binary-alloy solute rejection (Smith *et al* 1955) are clearly evident. The concentration at the centreline increases from $C/C_0 = 9.622$ at 3,000 s to 15.90 and 20.79 at 6,000 and 9,000 s respectively. The impact of convection on the solute profiles can also be seen in this plot. Warm, solute-poor fluid impinges on the top section of the interface. This fluid, cooled by the interface, falls toward the bottom wall and then returns to the bulk (refer to figure 5).

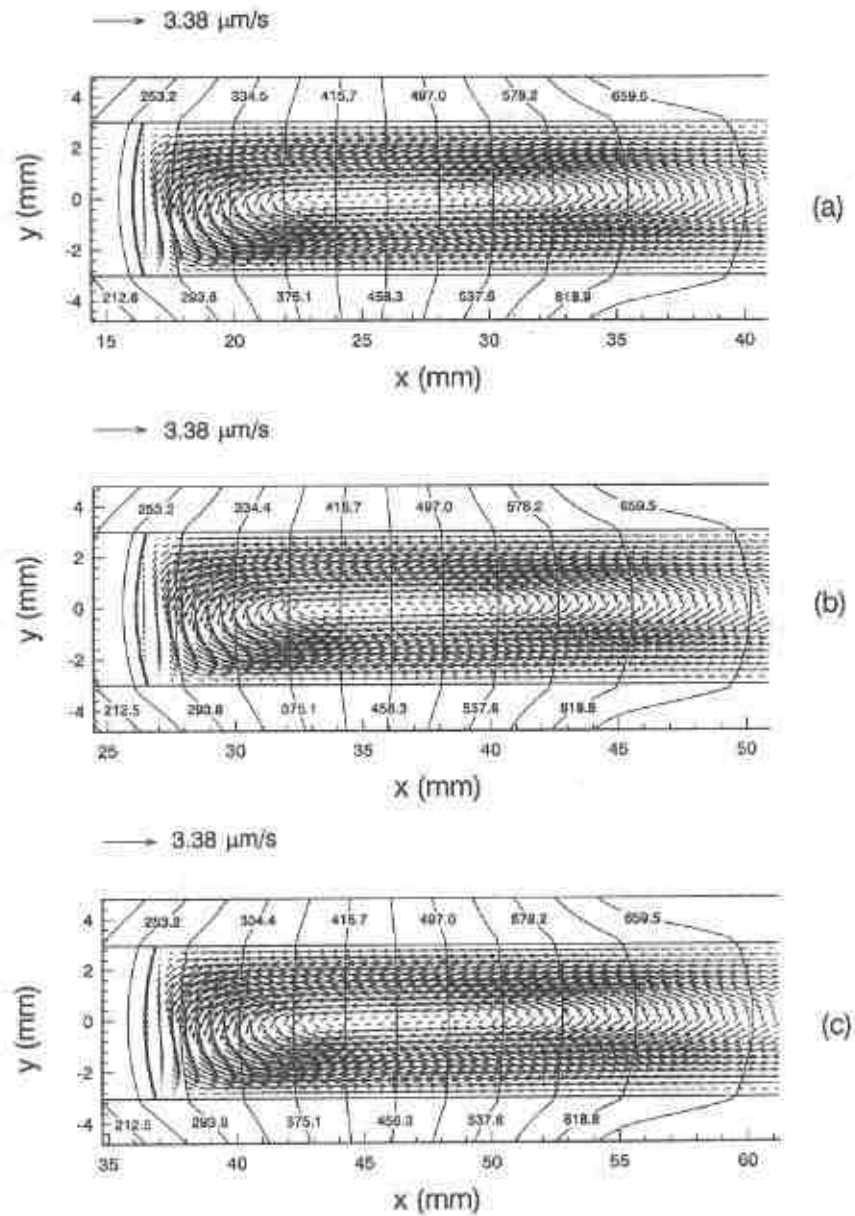


Figure 5. Velocity vectors and isotherms for the Bridgman growth of Bi-0.1 at.% Sn at (a) 3,000, (b) 6,000, and (c) 9,000 s. Thick solid line indicates location of solid/liquid interface.

It is this convective transport that causes a thinner solute boundary layer and lower interface concentration value in the $y = 2.88$ mm trace and, conversely, a thicker solute boundary layer and higher interface concentration value for the $y = -2.88$ mm trace. The interface concentration values along the centreline remain larger than those found at the periphery for all the times shown. This effect is due to interface curvature (see figure 6a). The traces in the solid indicate the level of axial segregation as the

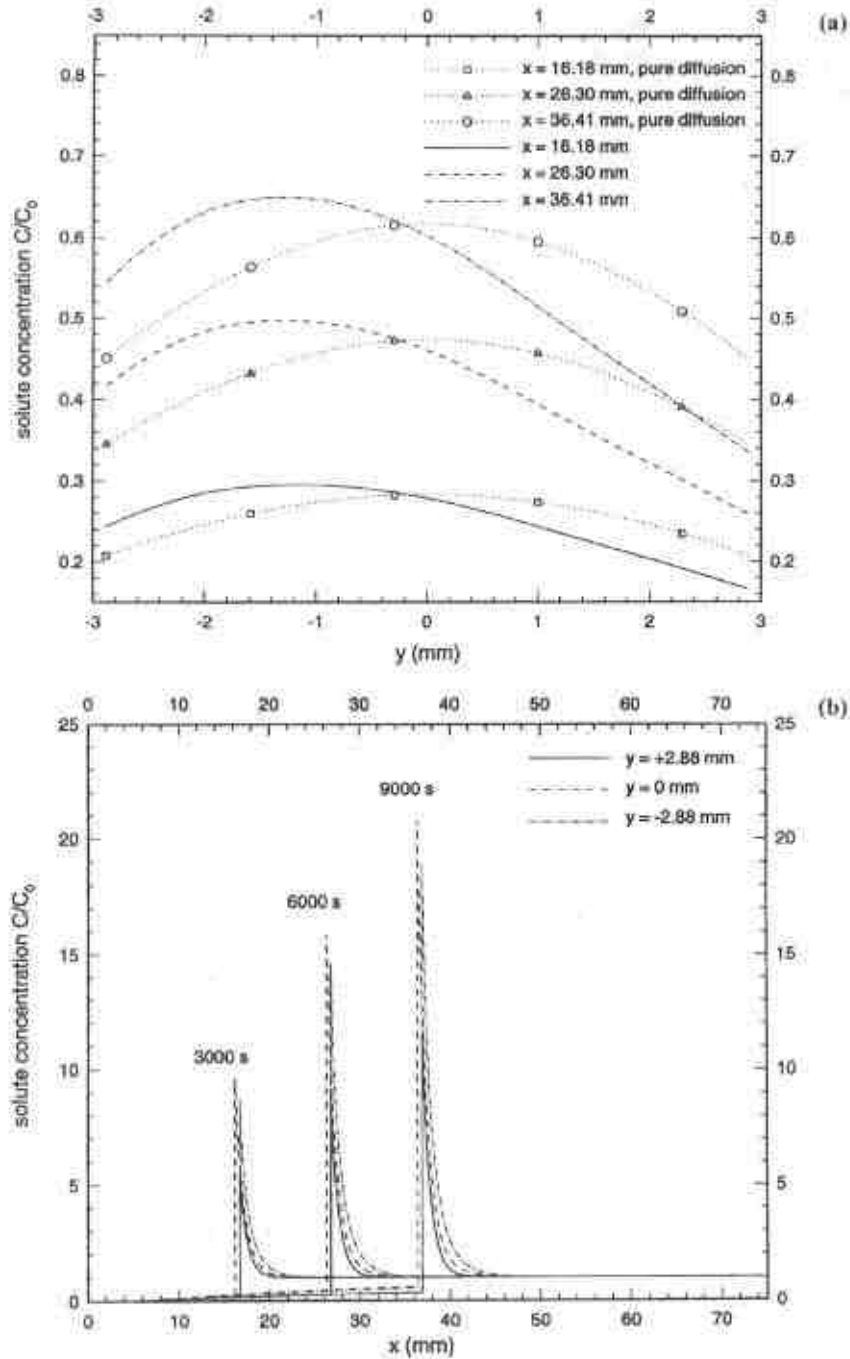


Figure 6. Solute concentrations for Bi-0.1 at.% Sn. (a) Traces across the solidified material at various x -locations. Dotted lines correspond to diffusion-only (no convection) results. Note that interface shape leads to radial segregation even in the absence of convection. (b) Longitudinal solute concentration traces at three different y -locations. In general, the solute boundary layers are larger for this case than for those in figure 8b, §3.4.

solute concentration in the solid increases with time, and also indicate the radial segregation evident in figure 6a.

For the low-concentration alloy, the solute concentration profiles are governed by solute rejection at the (curved) interface and by thermal convection only. The action of solutal convection is limited at these low concentrations. The velocity field indicates that thermal convection decreases slightly with time.

3.4 Space crystal growth of a Bi-1.0 at.% Sn alloy

A more solute-rich alloy was simulated next. The liquid composition was taken to be at a uniform value of 1.0 at.% Sn (0.8185 vol.% Sn) as the initial condition (yielding $Gr_s = 3.490$). The calculations for this case were the most intensive; the total CPU requirement was 21.3 h. The simulation was executed on a DEC Alphaserver 2100A (300 MHz, SPECfp95 14.0).

Velocity vectors and isotherms after 3,000 s for this alloy are shown in figure 7a. The velocity vectors indicate a primary convective cell rotating in a counter-clockwise manner in the translating zone, along with a weak secondary, clockwise convective cell driven by solute gradients adjacent to the interface. The two-cell convective motion is in contrast to that observed in figure 5a. The maximum v -velocity in the secondary convective cell near the interface at (16.5, 0 mm) is $0.5744 \mu\text{m/s}$. The nature of the maximum velocities differs from those shown in figure 5a; the maximum u -velocity for this case is $3.444 \mu\text{m/s}$ at (25.5, -1.8 mm), which is lower than the value of $3.467 \mu\text{m/s}$ found for the more dilute alloy. The maximum v -velocity magnitude is $-1.864 \mu\text{m/s}$ acting downward at (19.25, 0 mm), which is larger in magnitude than for the Bi-0.1 at.% Sn case ($-1.768 \mu\text{m/s}$). This maximum is located further from the interface ($x = 19.25$ mm versus $x = 17.75$ mm for pure and Bi-0.1 at.% Sn). Higher levels of solute rejection due to the higher initial concentration of the melt cause the formation of the secondary cell which is responsible for these effects.

At a later time (6,000 s), the front is at $x = 26.30$ mm, as shown in figure 7b. The secondary convective cell has increased in size and strength as solute – the driving force for this cell – continues to build up at the interface. The maximum v -velocity in the secondary convective cell near the interface is located above the centreline. Later in the growth process (9,000 s, figure 7c), the front has advanced to $x \approx 36.41$ mm, and the secondary convective cell has become quite strong.

Traces of solute concentration across the height of solidified alloy, along with pure diffusion results, are shown in figure 8a. This plot provides a stark contrast to the results shown for the more dilute alloy in figure 6a; the formation and growth of the secondary cell causes segregation to occur in the opposite sense (such that concentration values near the top of the domain are higher than at the bottom). For the trace at $x = 16.18$ mm, the concentration values are close to the values predicted from the pure diffusion analysis; the maximum value is $C/C_0 = 0.2812$ at $y = 0.05880$ mm with a segregation value of $\xi = 28.9\%$. This serendipitous result is a consequence of segregation arising from the influence of the secondary cell balancing segregation caused by the thermally driven cell when solidification has proceeded to this location. At lower values of x ($t < 3,000$ s), segregation is such that the maximum value occurs at $y < 0$ (similar to the Bi-0.1 at.% Sn alloy result, see figure 6a) while at higher values of x ($t > 3,000$ s) this maximum is shifted to a more positive y value. The traces at $x = 26.30$ and 36.41 mm show that

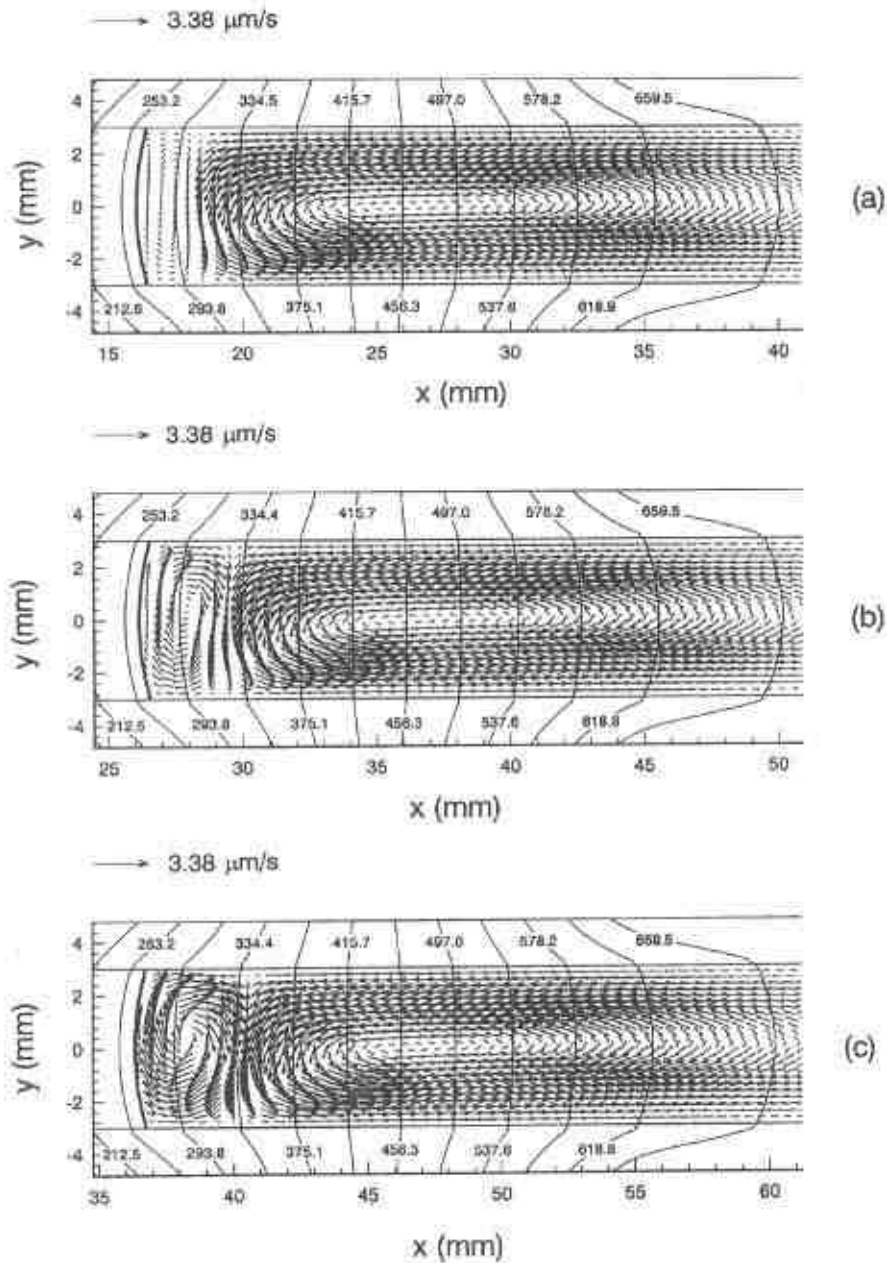


Figure 7. Velocity vectors and isotherms for the Bridgman growth of Bi-1.0 at % Sn at (a) 3,000, (b) 6,000 and (c) 9,000 s. Thick solid line indicates location of solid/liquid interface. A primary counter-clockwise convective cell, driven by thermal gradients, is evident in all three panels. A secondary, clockwise cell driven by solutal gradients develops with time.

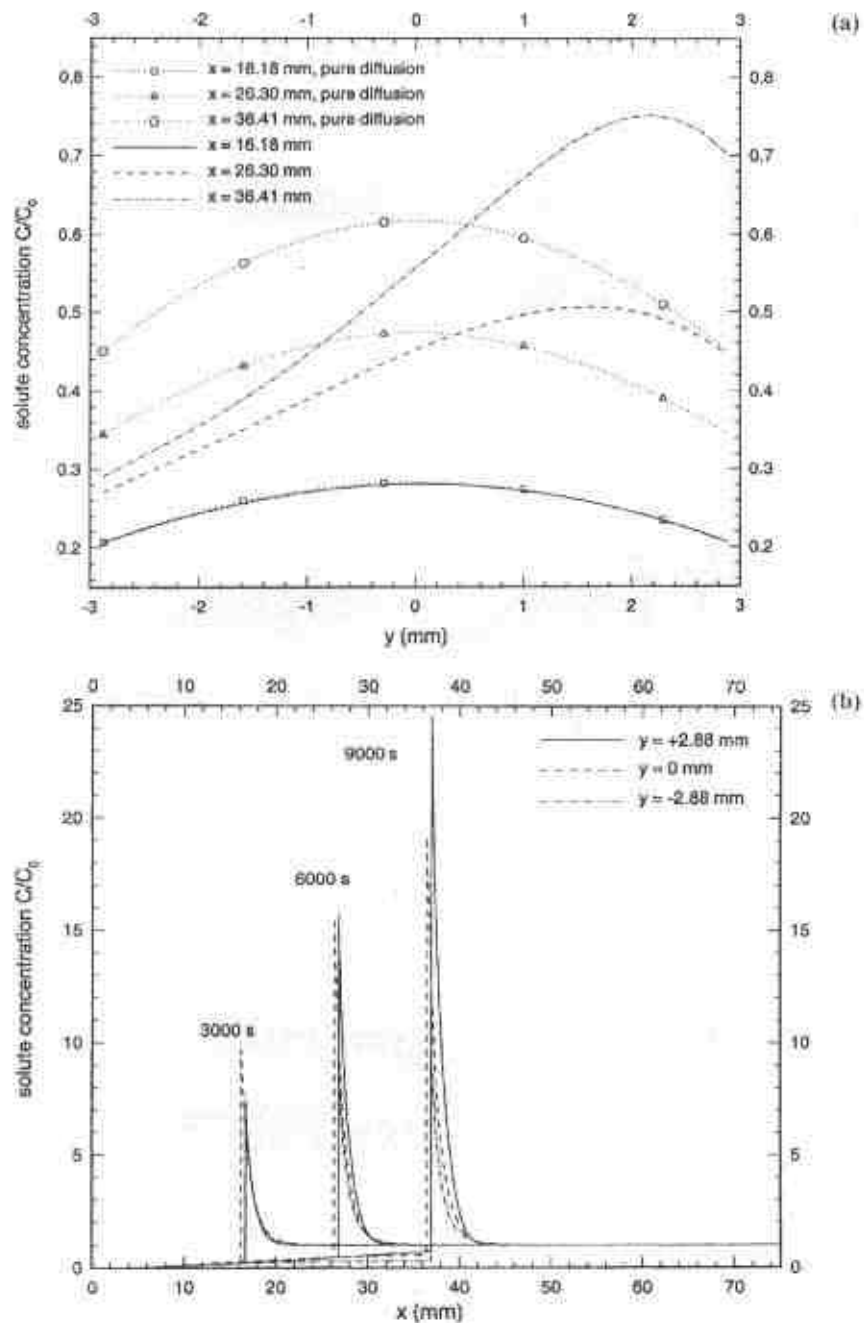


Figure 8. Solute concentrations for Bi-1.0 at.% Sn. (a) Traces across the solidified material at various x -locations. Dotted lines correspond to diffusion-only results. (b) Longitudinal solute concentration traces at three y -locations. The profiles are a result of combined diffusive and convective processes. Maximum concentration increases for each case, indicating solute build-up.

increasing solutal convection leads to increasing radial segregation. The maximum values are $C/C_0 = 0.5062$ and 0.7509 with radial segregation levels of $\xi = 54.7$ and 82.2% respectively. This behaviour is different from that shown in figure 6a, where the convective field remains almost steady with respect to the interface resulting in only a slight increase in segregation.

Figure 8b is a plot of longitudinal solute traces at domain heights of $y = -2.88, 0$ and 2.88 mm for the Bi-1.0 at.% Sn case at times of 3,000, 6,000 and 9,000 s. As for the case shown in figure 6b there is significant solute build-up, with values of liquid solute concentration C/C_0 at the interface along the centreline of 9.7, 15.59 and 19.20 respectively. Note, however, that this corresponds to much higher concentrations due to the higher initial concentration C_0 . Near the interface, the values for solute in the liquid are higher for $y = 2.88$ mm than that for $y = -2.88$ mm. Further from the solute interface, but still within the solute boundary layer, concentration increases with decreasing y . This is due to the interaction of the two convective cells. Nearer the interface, the secondary cell circulates solute-rich material within the boundary layer, acting to accumulate solute-rich material near the interface. Further from the interface (refer to figure 7), the primary convective cell influences the solute distribution, sweeping solute from the bottom of the domain into the bulk and thickening the solute boundary layer in this region. In general, the solute boundary layers are more compact than for the dilute alloy case at each corresponding time. Note that concentration values of this magnitude would be sufficient to lower the melting temperature of the alloy by a significant amount (see Simpson *et al* 1998). This effect may alter the concentration and velocity fields and is being addressed in ongoing work (Garimella & Simpson 2000).

For the higher alloy concentrations, solutal convection plays a much larger role, as can be seen in the concentration profiles discussed above. As growth proceeds, the level of solutal convection grows, with a corresponding increase in radial segregation. The maximum concentration increases much more rapidly than the minimum value.

4. Conclusions

A fully transient, fixed-grid method for the efficient solution of convection-conduction phase change problems has been used to highlight the pivotal role of thermosolutal convection in macrosegregation.

Results for the directional solidification of pure tin as well as a dilute Sn-Bi alloy (at a high Rayleigh number and low Prandtl number) under terrestrial conditions were presented. The results were found to agree well with experimental data (Wolff & Viskanta 1988) and with numerical solutions (Raw & Lee 1991; Zhang *et al* 1996); these results also indicated that the strong levels of convection present drastically alter the distribution of solute in the melt region and therefore in the solidified material.

Simulations of horizontal Bridgman crystal growth in microgravity conditions were then discussed. For the dilute alloy simulation (Bi-0.1 at.% Sn), a single dominant counter-clockwise rotating convective cell was present for the entire duration. With increasing time, solute was rejected at the interface and the level of solute near the interface increased. Due to the presence of convection, radial solute segregation occurred with preferentially higher values at the bottom of the solid. The level of segregation increased slightly with time. The maximum values of concentration were small and so the assumption of constant alloy melting temperature was realistic.

For the richer alloy (Bi-1.0 at.% Sn), the convective field was much more complex. Higher levels of solute rejection at the interface caused higher levels of solutal convection. Initially, a single, thermally driven, counter-clockwise rotating cell was present. As time proceeded and solute accumulated at the interface, a secondary, solute-driven clockwise rotating cell developed. The effect of this convective pattern was to cause significant levels of segregation in the solute at the interface (and hence in the solid). This segregation was such that the values toward the top of the domain were maximum. The higher values of concentration near the interface resulted in a significant change in the melting temperature for the alloy. Investigating the effects of concentration-dependent melting temperature is being addressed in ongoing work.

List of symbols

c_p	specific heat at constant pressure;
C	species concentration;
D	species diffusion coefficient;
f	volume fraction;
g	acceleration due to gravity;
Gr	Grashof number, $g\beta_T(T_H-T_C)L_R^3/\nu^2$;
Gr_s	solutal Grashof number, $g\beta_s C_0 L_R^3/\nu^2$;
h	ampoule thickness (outside radius – inside radius);
H	domain height (figure 1a) or ampoule diameter (figure 1b);
k	thermal conductivity;
k_p	segregation coefficient;
L	length of simulation domain;
L_A	translating zone length;
L_R	reference length (L for terrestrial solidification problem, H for crystal growth problem);
Le	Lewis number, α/D ;
Pr	Prandtl number, ν/α ;
Ra	Rayleigh number ($= Gr \times Pr$);
R_B	bouyancy ratio ($= Gr_s/Gr$);
t	time;
T	temperature;
u, v, w	velocities in x, y, z directions;
β	expansion coefficient;
ΔT	temperature difference, $T_H - T_C$;
ΔH	enthalpy of freezing;
ζ	vorticity;
θ	nondimensional temperature, $(T - T_c)/(T_H - T_c)$;
μ	dynamic viscosity;
ν	kinematic viscosity;
ξ	radial segregation, $(C_{max} - C_{min})/C_{average}$;
ρ	density;
ψ	stream function.
<i>Subscripts</i>	
0	initial condition;
C	cold furnace temperature condition;

H	hot furnace temperature condition;
L	liquid;
m	at solidification front;
S	solid;
w	ampoule wall.

Superscripts

$\hat{}$	unit vector;
\sim	vector.

References

- Adornato P M, Brown R A 1987 Convection and segregation in directional solidification of dilute and non-dilute binary alloys. *J. Crystal Growth* 80: 155–190
- Dantzig J A 1989 Modelling liquid-solid phase changes with melt convection. *Int. J. Numer. Meth. Engng* 28: 1769–1785
- Flemings M C, Nereo G E 1967 Macrosegregation: Part I. *Trans. Metal. Soc. AIME* 229: 1449–1461
- Garimella S V, Simpson J E 2000 Numerical investigations of alloy solidification in space. *Proc. ISHMT/ASME Joint Heat and Mass Transfer Conference*, Pune (New Delhi: Tata-McGraw Hill) pp 243–249
- Hirasaki G J, Hellums J D 1968 A general formulation of the boundary conditions on the vector potential in three dimensional hydrodynamics. *Q. Appl. Math.* 16: 331–342
- Hyun M T, Kuo D C, Bergman T L, Ball K S 1995 Direct simulation of double diffusion in low Prandtl number liquids. *Numer. Heat Transfer* A27: 639–650
- Liang M C, Lan C W 1996 Three-dimensional convection and solute segregation in vertical Bridgman crystal growth. *J. Crystal Growth* 167: 320–332
- Oldenburg C M, Spera F J 1991 Numerical modeling of solidification and convection in a viscous pure binary eutectic system. *Int. J. Heat Mass Transfer* 34: 2107–2121
- Raw W Y, Lee S L 1991 Application of weighting function scheme on convection-conduction phase change problems. *Int. J. Heat Mass Transfer* 34: 1503–1513
- Roache P J 1976 *Computational fluid dynamics* (Hermosa)
- Simpson J E, Garimella S V 1998 An investigation of the solutal, thermal and flow fields in unidirectional alloy solidification. *Int. J. Heat Mass Transfer* 41: 2485–2502
- Simpson J E, Garimella S V 2000 The influence of gravity levels on the horizontal bridgman crystal growth of an alloy. *Int. J. Heat Mass Transfer* 11: 1905–1923
- Simpson J E, Yao M, de Groh H C III, Garimella S V 1998 Numerical modeling of solidification in space with MEPHISTO-4 (Part 2). NASA Tech. Mem. TM-1998-206630
- Simpson J E, Garimella S V, de Groh H C III, Abbaschian R 1999 Numerical simulation of crystal growth of an alloy under microgravity conditions. *Proc. Natl. Heat Trans. Conf.*, (ASME) NHTC99-204 pp 1–9
- Simpson J E, de Groh H C III, Garimella S V 1999b An experimental and computational study of directional solidification in transparent materials. In *Fluid flow phenomena in metals processing* (eds) N El-Kaddah *et al* (Warrendale, PA: TMS) pp 449–458
- Simpson J E, de Groh H C III, Garimella S V 1999c Directional solidification of pure succinonitrile and a succinonitrile-acetone alloy. NASA Tech. Mem. TM-1999-209381
- Simpson J E, Garimella S V, de Groh H C III, Abbaschian R 2001 Bridgman crystal growth of an alloy with thermosolutal convection under microgravity conditions. *ASME J. Heat Transfer* (in press)
- Smith V G, Tiller W A, Rutter J W 1955 A mathematical analysis of solute redistribution during solidification. *Can. J. Phys.* 33: 723–743

- Swaminathan C R, Voller V R 1997 Towards a general numerical scheme for solidification systems. *Int. J. Heat Mass Transfer* 30: 2859–2868
- Voller V R, Brent A D, Prakash C 1989 The modelling of heat, mass and solute transport in solidification systems. *Int. J. Heat Mass Transfer* 32: 1719–1731
- Wolff F, Viskanta R 1988 Solidification of a pure metal at a vertical wall in the presence of liquid superheat. *Int. J. Heat Mass Transfer* 31: 1735–1744
- Yao M, Raman R, de Groh H C III 1995 Numerical modeling of Bridgman growth in space with MEPHISTO. In *Computational mechanics '95, Proc. Int. Conf. Computational Engineering Science* (Springer) vol. 1, pp. 514–519; also NASA Tech. Mem. #107015
- Zeng X, Faghri A 1994 Temperature-transforming model for binary solid-liquid phase-change problems, Part 1: Mathematical modeling and numerical methodology. *Numer. Heat Transfer* B25: 467–480
- Zhang H, Prasad V, Moallemi M K 1996 Numerical algorithm using multizone adaptive grid generation for multiphase transport processes with moving and free boundaries. *Numer. Heat Transfer* B29: pp. 399–421